Title

DESI Strong Lens Foundry. III. Keck Spectroscopy for Strong Lenses Discovered Using Residual Neural Networks

Journal

The Astrophysical Journal, 1001(2)

ISSN

0004-637X

Authors

Agarwal, Shrihan
Huang, Xiaosheng
Sheu, W
et al.

Publication Date

2026-04-20

DOI

10.3847/1538-4357/ae4a9a

THE ASTROPHYSICAL JOURNAL, 1001:162 (13pp), 2026 April 20 https://doi.org/10.3847/1538-4357/ae4a9a

DESI Strong Lens Foundry. III. Keck Spectroscopy for Strong Lenses Discovered Using Residual Neural Networks

Shrihan Agarwal[1,2,3], Xiaosheng Huang[3,4], W. Sheu[3,5], C.J. Storfer[6], M. Tamargo-Arizmendi[7], S. Tabares-Tarquinio[3,4], D.J. Schlegel[8], G. Aldering[3], A. Bolton[8], A. Cikota[9], Arjun Dey[8], A. Filipp[10,11,12,13], E. Jullo[14], K.J. Kwon[15], S. Perlmutter[3,16], Y. Shu[17], E. Sukay[18], N. Suzuki[3,19], J. Aguilar[20], S. Ahlen[21], S. BenZvi[22], D. Brooks[23], T. Claybaugh[20], P. Doel[23], J. E. Forero-Romero[24,25], E. Gaztañaga[26,27,28], S. Gontcho A Gontcho[20], G. Gutierrez[29], K. Honscheid[30,31,32], M. Ishak[33], S. Juneau[34], R. Kehoe[35], T. Kisner[20], S. E. Koposov[36,37], A. Lambert[20], M. Landriau[20], L. Le Guillou[38], A. de la Macorra[39], A. Meisner[34], R. Miquel[40,41], J. Moustakas[42], A. D. Myers[43], C. Poppett[20,44,45], F. Prada[46], I. Pérez-Ràfols[47], G. Rossi[48], E. Sanchez[49], M. Schubnell[50,51], D. Sprayberry[34], G. Tarlé[51], B. A. Weaver[34], and H. Zou[52]

[1] University of Chicago, Department of Astronomy, Chicago, IL 60615, USA; shrihan@uchicago.edu
[2] University of California, Berkeley, Department of Astronomy, Berkeley, CA 94720, USA
[3] Physics Division, Lawrence Berkeley National Laboratory, 1 Cyclotron Road, Berkeley, CA 94720, USA; xhuang22@usfca.edu
[4] Department of Physics & Astronomy, University of San Francisco, San Francisco, CA 94117, USA
[5] Department of Physics & Astronomy, University of California, Los Angeles, Los Angeles, CA 90095, USA
[6] Institute for Astronomy, University of Hawai'i, Honolulu, HI 96822-1897, USA
[7] Department of Physics and Astronomy and PITT PACC, University of Pittsburgh, Pittsburgh, PA 15260, USA
[8] NSF's National Optical-Infrared Astronomy Research Laboratory, 950 N. Cherry Ave., Tucson, AZ 85719, USA
[9] Gemini Observatory / NSF's NOIRLab, Casilla 603, La Serena, Chile
[10] Université de Montréal, Physics Department, 1375 Av. Thérèse-Lavoie-Roux, H2V 0B3 Montréal, QC, Canada
[11] Ciela – Montreal Institute for Astrophysical Data Analysis and Machine Learning, 1375 Av. Thérèse-Lavoie-Roux, H2V 0B3 Montréal, QC, Canada
[12] Technical University Munich, TUM School of Natural Sciences, Physics Department, 85748 Garching, Germany
[13] Max Planck Institute for Astrophysics (MPA), Karl-Schwarzschild-Strasse 1, 85748 Garching, Germany
[14] Aix-Marseille Univ., CNRS, CNES, LAM, Marseille, France
[15] University of California, Santa Barbara, Santa Barbara, CA 93106, USA
[16] Department of Astronomy, University of California, Berkeley, CA 94720, USA
[17] Purple Mountain Observatory, Chinese Academy of Sciences, Nanjing 210023, People's Republic of China
[18] Johns Hopkins University, Department of Physics & Astronomy, Baltimore, MD 21218, USA
[19] Kavli Institute for the Physics and Mathematics of the Universe, University of Tokyo Kashiwa 277-8583, Japan
[20] Lawrence Berkeley National Laboratory, 1 Cyclotron Road, Berkeley, CA 94720, USA
[21] Physics Dept., Boston University, 590 Commonwealth Avenue, Boston, MA 02215, USA
[22] Department of Physics & Astronomy, University of Rochester, 206 Bausch and Lomb Hall, P.O. Box 270171, Rochester, NY 14627-0171, USA
[23] Department of Physics & Astronomy, University College London, Gower Street, London, WC1E 6BT, UK
[24] Observatorio Astronómico, Universidad de los Andes, Cra. 1 No. 18A-10, Edificio H, CP 111711 Bogotá, Colombia
[25] Departamento de Física, Universidad de los Andes, Cra. 1 No. 18A-10, Edificio Ip, CP 111711, Bogotá, Colombia
[26] Institute of Cosmology and Gravitation, University of Portsmouth, Dennis Sciama Building, Portsmouth, PO1 3FX, UK
[27] Institute of Space Sciences, ICE-CSIC, Campus UAB, Carrer de Can Magrans s/n, 08913, Bellaterra, Barcelona, Spain
[28] Institut d'Estudis Espacials de Catalunya (IEEC), c/ Esteve Terradas 1, Edifici RDIT, Campus PMT-UPC, 08860 Castelldefels, Spain
[29] Fermi National Accelerator Laboratory, PO?Box 500, Batavia, IL 60510, USA
[30] The Ohio State University, Columbus, 43210 OH, USA
[31] Center for Cosmology and AstroParticle Physics, The Ohio State University, 191 West Woodruff Avenue, Columbus, OH 43210, USA
[32] Department of Physics, The Ohio State University, 191 West Woodruff Avenue, Columbus, OH 43210, USA
[33] Department of Physics, The University of Texas at Dallas, 800 W. Campbell Rd., Richardson, TX 75080, USA
[34] NSF NOIRLab, 950 N. Cherry Ave., Tucson, AZ 85719, USA
[35] Department of Physics, Southern Methodist University, 3215 Daniel Avenue, Dallas, TX 75275, USA
[36] Institute for Astronomy, University of Edinburgh, Royal Observatory, Blackford Hill, Edinburgh EH9 3HJ, UK
[37] Institute of Astronomy, University of Cambridge, Madingley Road, Cambridge CB3 0HA, UK
[38] Sorbonne Université, CNRS/IN2P3, Laboratoire de Physique Nucléaire et de Hautes Energies (LPNHE), FR-75005 Paris, France
[39] Instituto de Física, Universidad Nacional Autónoma de México, Circuito de la Investigación Científica, Ciudad Universitaria, Cd. de México C. P. 04510, Mexico
[40] Institut de Física d'Altes Energies (IFAE), The Barcelona Institute of Science and Technology, Edifici Cn, Campus UAB, 08193, Bellaterra (Barcelona), Spain
[41] Institució Catalana de Recerca i Estudis Avançats, Passeig de Lluís Companys, 23, 08010 Barcelona, Spain
[42] Department of Physics and Astronomy, Siena College, 515 Loudon Road, Loudonville, NY 12211, USA
[43] Department of Physics & Astronomy, University of Wyoming, 1000 E. University, Dept. 3905, Laramie, WY 82071, USA
[44] Space Sciences Laboratory, University of California, Berkeley, 7 Gauss Way, Berkeley, CA 94720, USA
[45] University of California, Berkeley, 110 Sproul Hall #5800 Berkeley, CA 94720, USA
[46] Instituto de Astrofísica de Andalucía (CSIC), Glorieta de la Astronomía, s/n, E-18008 Granada, Spain
[47] Departament de Física, EEBE, Universitat Politècnica de Catalunya, c/Eduard Maristany 10, 08930 Barcelona, Spain
[48] Department of Physics and Astronomy, Sejong University, 209 Neungdong-ro, Gwangjin-gu, Seoul 05006, Republic of Korea
[49] CIEMAT, Avenida Complutense 40, E-28040 Madrid, Spain

[50] Department of Physics, University of Michigan, 450 Church Street, Ann Arbor, MI 48109, USA
[51] University of Michigan, 500 S. State Street, Ann Arbor, MI 48109, USA
[52] National Astronomical Observatories, Chinese Academy of Sciences, A20 Datun Rd., Chaoyang District, Beijing, 100012, People's Republic of China
Received 2025 June 5; revised 2026 January 24; accepted 2026 February 24; published 2026 April 14

Abstract

We present spectroscopic data of strong lenses and their source galaxies using the Keck Near-Infrared Echellette Spectrometer (NIRES) and the Dark Energy Spectroscopic Instrument (DESI), providing redshifts necessary for nearly all strong-lensing applications with these systems, especially the extraction of physical parameters from lensing modeling. These strong lenses were found in the DESI Legacy Imaging Surveys using residual neural networks and followed up by our Hubble Space Telescope program, with all systems displaying unambiguous lensed arcs. With NIRES, we target eight lensed sources at redshifts difficult to measure in the optical range and determine the source redshifts for six, between $z_s = 1.675$ and 3.332. DESI observed one of the remaining source redshifts, as well as an additional source redshift within the six systems. The two systems with nondetections by NIRES were observed for a considerably shorter 600 s at high airmass. Combining NIRES infrared spectroscopy with optical spectroscopy from our DESI Strong Lensing Secondary Target Program, these results provide the complete lens and source redshifts for six systems, a resource for refining automated strong lens searches in future deep- and wide-field imaging surveys and addressing a range of questions in astrophysics and cosmology.

Unified Astronomy Thesaurus concepts: Strong gravitational lensing (1643); Gravitational lensing (670); Galaxy spectroscopy (2171); Infrared spectroscopy (2285); Spectroscopy (1558); High-redshift galaxies (734)

1. Introduction

As a consequence of general relativity, foreground galaxies or galaxy clusters can warp spacetime and bend the light of background galaxies when the alignment is nearly perfect, resulting in the formation of multiple images, arcs, or Einstein rings (e.g., D. Walsh et al. 1979; J. Huchra et al. 1985; A. S. Bolton et al. 2008). These strong gravitational lensing systems offer significant insights into astrophysics and cosmology. Since the deflection of light is a function of the lens mass, these systems may be used to study the distribution of dark matter in lensing galaxies and galaxy clusters (e.g., C. S. Kochanek 1991; L. V. E. Koopmans & T. Treu 2002; A. S. Bolton et al. 2006; D. Clowe et al. 2006; L. V. E. Koopmans et al. 2006; M. Bradač et al. 2008; X. Huang et al. 2009; E. Jullo et al. 2010; C. Grillo et al. 2015; Y. Shu et al. 2015, 2016a, 2016b, 2017; N. Tessore et al. 2016), as well as dark matter substructure or line-of-sight low-mass halos (e.g., S. Vegetti et al. 2010; Y. D. Hezaveh et al. 2016; A. Ç. Çağan Şengül et al. 2022). These systems also act as a magnifying glass for both spectral and spatial features of the lensed background galaxy, allowing more detailed study of the morphology of high-redshift galaxies (e.g., P. J. Marshall et al. 2007; M. A. Cornachione et al. 2018; V. Patrício et al. 2019; E. Vanzella et al. 2020). Finally, multiple images of a transient in the background galaxy (typically a quasar or supernova) can be used to measure time delays, providing an independent measurement of the Hubble constant H_0 (e.g., D. A. Goldstein & P. E. Nugent 2017; D. A. Goldstein et al. 2018; Y. Shu et al. 2018; J. D. R. Pierel & S. Rodney 2019; R. Wojtak et al. 2019; S. H. Suyu et al. 2020; P. L. Kelly et al. 2023; S. H. Suyu et al. 2024).

We conducted searches for strong lensing systems (X. Huang et al. 2020, 2021; C. Storfer et al. 2024) using deep residual neural networks (ResNet; K. He et al. 2015) on the Dark Energy Spectroscopic Instrument (DESI) Legacy Imaging Surveys (A. Dey et al. 2019), and presented a large catalog of ∼3500 new strong lens candidates.[53] These candidate systems need follow-up observations for confirmation. For high-resolution imaging, our Hubble Space Telescope (HST) Snapshot program followed up on a subset of 51 candidates. Except for one ambiguous case, 50 of 51 candidates in our HST sample show unambiguous arcs, with most having multiple lensed images (Paper I in this series, X. Huang et al. 2026). Spectroscopic observations are also being carried out. A. Cikota et al. (2023) published the first of our candidate systems spectroscopically confirmed by VLT MUSE. The Dark Energy Spectroscopic Experiment (DESI Collaboration et al. 2016a, 2016b) Strong Lensing Secondary Target Program has already observed a large fraction of our lens candidates for spectroscopic confirmation within its footprint.[54] Paper II in this series (X. Huang et al. 2025b) will introduce this program and present strong lensing spectra from DESI Early Data Release.

For a fraction of the systems in our lens candidate catalog (preliminarily, ∼30%), the source redshifts are too high and the typical emission features (e.g., [O II] 3727) would lie beyond the optical range. We therefore turn to Keck NIRES to obtain spectroscopic redshifts for the lensed sources of these systems. Of these 30% of systems, the selection criteria for the eight systems in this paper were primarily based on visibility from Keck, the typical airmass of observation, and the brightness of the lensed arcs. Follow-up studies on the remaining systems are underway, and multiple Keck observing runs have been completed. Here, in Paper III of this series, we present our first near-IR spectroscopic follow-up results from Keck NIRES for systems observed by our HST program. We describe our Keck NIRES observations in Section 2, and present the data reduction pipeline in

[53] The entire catalog of these lens candidates can be found on our project website: https://sites.google.com/usfca.edu/neuralens/

[54] DESI will separately follow up lensed quasar candidates discovered by autocorrelation (C. Dawes et al. 2023)

Section 3. We describe our results in Section 4, and conclude in Section 5.

2. Observations

2.1. Hubble Space Telescope

For our Hubble Space Telescope Snapshot program (GO-15867, PI: Huang), *Confirming Strong Galaxy Gravitational Lenses in the DESI Legacy Imaging Surveys*, we submitted a subset of our most promising lens candidates (112 targets). Details of the program are provided in Paper I (X. Huang et al. 2026) of this series. Briefly, 51 systems were observed by WFC3 in F140W, with approximately half galaxy-scale and half group-scale lensing systems. Fifty out of 51 of them were confirmed to be strong lenses based on unambiguous lensing features in the high-resolution HST images. Our Keck NIRES observations described below target a subset of these systems. Hubble Space Telescope data for these systems are hosted online.[55]

2.2. Keck NIRES

To fully characterize a lensing system, we need to measure the redshifts of both the lens deflector (z_d) and lensed source (z_s). DESI has been highly successful in obtaining lens redshifts (Paper II, X. Huang et al. 2025b), since lens spectra commonly have prominent absorption features (e.g., Ca H&K) and the 4000 Å Balmer break, within its optical range ($z_d \lesssim 1.6$). However, for 7 of the 8 systems in this paper, DESI was unable to obtain the source redshifts as of DESI DR2, likely since all these features, including the strong [O II] doublet emission feature, are redshifted beyond its optical range into the infrared. We therefore target these lensed sources using NIR spectroscopy, namely the NIRES instrument (J. C. Wilson et al. 2004) on the 10 m Keck II Telescope.[56] Lensed source galaxies, being at higher redshifts, are typically star-forming (e.g., A. S. Bolton et al. 2006). NIRES provides broad wavelength coverage in the near-infrared that can be used to identify emission features of these source galaxies and secure their redshift. NIRES is a cross-dispersed echellette spectrograph, covering a wavelength range of 0.94–2.45 μm including the *Y*, *J*, *H*, and *K* bands. NIRES has five spectral orders with overlap, the only gap being between 1.85–1.88 μm, a region of poor atmospheric transmission. The slit size is $0\farcs55 \times 18''$, with an average spectral resolution of $\lambda/\Delta\lambda \approx 2700$ ($\Delta v \approx 110\,\mathrm{km\ s^{-1}}$) and spectrometer pixel scale of $0\farcs15\ \mathrm{pix}^{-1}$.

A total of eight systems from X. Huang et al. (2020, H20) and X. Huang et al. (2021, H21) that were observed and confirmed to be strong lenses by HST were followed up by Keck NIRES over two half-nights.[57] In this Keck NIRES program, our primary goal is to measure the source redshifts. Therefore, our slits were oriented accordingly along the brightest source arc images, typically on high star formation rate regions ("knots") within them. The target name, date of observation, coordinates, exposure length, and other relevant observing information are provided in Table 1. Observations of the science targets as well as the standard star were conducted with an ABBA dither pattern with a $2''$–$4''$ nod depending on the extent of the arcs and their positions in the slit.[58] This allows a subtraction of correlated noise pattern in the spectrum by subtracting the A and B dithers. For all systems in this paper, each dither had an exposure time of 300 s, and so a full ABBA set requires a 1200 s total exposure. The two systems DESI J023.0157–16.0040 and DESI J024.1631+00.1384 were observed at a high airmass of ≈1.6. After a 600 s AB exposure each, we decided to move to the next target, as we were unconvinced we could secure the redshift with the lack of visible emission features in the 2D spectrum and worsening airmass. These are the only two systems for which Keck NIRES was unable to secure a source redshift. The source redshift of DESI J023.0157–16.0040 was later captured successfully by DESI.

We provide the magnitudes of the star-forming knots for the lensed source images of each target in Table 1. They are calculated for the HST F140W band in the AB system, with a zero point of 26.45 (V. Bajaj et al. 2020). We calculate isophotal magnitudes using the total flux within a contour around a knot. We define the contour for each knot to be at 75% of the peak pixel value of the knot. Since a dim, extended region and a bright concentrated region may have similar magnitudes, we also provide the area within the contour as a proxy for the extent of the knot. For the two knots of DESI J023.0157–16.0040 and the fainter of the two knots covered by the slit in DESI J154.5307–00.1368, due to the presence of the lens light, the 75% contours also enclose a large fraction of the lens light. For these cases, we instead use an elliptical aperture placed over the knot at the 75% level as judged by the source image light profile at the far side relative to the lens location. The magnitude estimated this way thus is a lower bound for its true magnitude. More accurate photometry will be provided with full lens modeling, which will include the modeling of lens light, in future publications.

3. Spectral Reduction

We use PypeIt for spectral reduction. We introduce this open-source package in Section 3.1, and our reduction process in Section 3.2.

3.1. PypeIt

PypeIt is a versatile Python package for semi-automated reduction of spectroscopic data (J. Prochaska et al. 2020a; J. X. Prochaska et al. 2020b). The reduction takes several steps. First it performs overscan subtraction, dark-current and bias correction, bad pixel masking, slit edge detection, and wavelength calibration on both the science and standard star observations. Finally, PypeIt performs Poisson-limited sky subtraction and object extraction to generate the 1D and 2D science spectra. Object detection is typically done automatically, but for faint galaxies, where redshift measurements depend on emission-line detection, a manually laid trace is used to extract the spectra. These science spectra can be flexure corrected, coadded, and even telluric corrected. For

[55] 10.17909/d1yz-ze43

[56] We note that deeper optical spectroscopy (e.g., A. Cikota et al. 2023) remains an alternate method for follow-up at these redshifts.

[57] We were unable to observe on another half-night awarded to us, on 2022 December 16, due to weather.

[58] The ABBA dither pattern refers to taking exposures at the first dither position (A) and then two at the second dither position (B) before returning to position A. For further information, see NIRES Instrument Documentation: Observing Procedures (https://www2.keck.hawaii.edu/inst/nires/night_check.html).

Table 1
Keck NIRES Observations

Date	Seeing	Airmass	Target	R.A.	Decl.	Isophotal Magnitude	Contour Area	Exp. Time (s)
2022 Nov 13,	0."55	1.38	DESI J006.3643+10.1853	6.3643	+10.1853	23.84 ± 0.02	0.0325	1200
						23.87 ± 0.02	0.0450	
		1.60	DESI J023.0157–16.0040	23.0157	−16.0040	24.02 ± 0.02*	0.1014	600
						23.23 ± 0.02*	0.1436	
		1.56	DESI J024.1631+00.1384	24.1631	+0.1384	22.78 ± 0.01	0.1925	600
						22.71 ± 0.01	0.2425	
		1.18	DESI J094.5639+50.3059	94.5639	+50.3059	23.85 ± 0.02	0.0775	3600
						24.36 ± 0.03	0.0325	
		1.43	DESI J154.5307–00.1368	154.5307	−0.1368	24.24 ± 0.03*	0.1050	2400
						25.03 ± 0.04	0.0350	
2023 Jan 10,	0."8	1.07	DESI J133.3800+23.3652	133.3800	+23.3652	23.51 ± 0.02	0.0350	2400
						23.34 ± 0.02	0.0525	
		1.17	DESI J165.4754–06.0423	165.4754	−6.0423	22.15 ± 0.01	0.4775	3600
						22.28 ± 0.01	0.3725	
		1.11	DESI J215.2654+00.3719	215.2654	+0.3719	24.15 ± 0.03	0.0925	2400
						24.41 ± 0.03	0.0800	

Notes. The target naming convention is R.A. and decl. in decimal format. This naming convention differs slightly from past papers with candidates (X. Huang et al. 2020, 2021) where, e.g., DESI J006.3643+10.1853 is called DESI-006.3643+10.1853. We use the new convention for confirmed strong lenses, and also to match IAU naming conventions. The isophotal magnitude (mag) is for HST F140W in the AB system. The area of the contour in arcsec^2 is shown as a proxy for the extent of the star-forming region. *For these cases, the reported magnitudes are the lower (or brighter) bounds (see text), and only the uncertainties are shown.

further information regarding PypeIt, we direct the reader to J. Prochaska et al. (2020a) and J. X. Prochaska et al. (2020b).

3.2. Data Processing

For this paper, the spectra taken for each night consisted of science observations of the lensed sources and standard star observations from the CALSPEC database (R. C. Bohlin et al. 2014). Flat frames (120 s × 10) and dark frames (120 s × 10) were taken for calibration. Wavelength calibration was performed using sky lines.[59] PypeIt v1.13.0 was used for this analysis. Applying PypeIt to a broad range of spectra requires appropriate manual adjustments for our specific use case: spectroscopic extraction of source galaxy emission lines.

The main differences between our procedure and a standard PypeIt reduction are the use of a manual object extraction and the omission of a telluric correction. The continuum of the lensed source arcs typically does not have sufficient signal to be separated from noise. This means the emission features are not easily detected by PypeIt using the automatic object detection, and requires the manual specification of the object position and an estimation of the FWHM. Additionally, the automatic extraction routine had to be suppressed for a particular system (Section 4.3). This suppression was later adopted for all systems. Telluric correction is not used, due to the low signal-to-noise ratio (SNR) for our spectra (J. Hennawi 2026, private communication). At low SNR, this correction exhibits pathological behaviors, as it is challenging to distinguish noise from signal. This is acceptable, since for our targets, the telluric correction does not impact the redshift determination based on identifying emission features.

The standard star used to generate the sensitivity function for both nights was of the G191-B2B observations from the night of 2023 January 10.[60] These were taken with an exposure time of 15 s each in an ABBA dither pattern of 2″. Using the estimate of the sensitivity function from a different night may slightly affect line ratios, but should not impact redshift measurements. The ABBA frames of the emission-line spectra are individually extracted and coadded with their positive and negative features using PypeIt's weighted 1D coaddition pipeline (J. X. Prochaska et al. 2020b). PypeIt internally performs both correction of the spectra to the barycentric frame as well as to their vacuum wavelengths.

For all systems, we place the NIRES slit orientation along a lensed arc of the source galaxy in order to capture in the same slit two lensed images of the same star formation region or two different star formation regions (Sections 4.1 and 4.4) of the source galaxy. Therefore, the detected emission features have identical (or very similar (Section 4.4)) redshifts, allowing us to coadd their individual emission spectra. The combined 1D spectra are inspected alongside the 2D spectra (see, e.g., Figure 1).

3.3. Redshift Fitting

Redshift fitting was performed by performing a Gaussian fit to two emission lines in the spectrum. The two emission lines chosen are either the strongest emission lines or the strongest from two different elements, e.g., O and H. The fit involved six parameters. The redshift z, which determines the mean wavelengths of the Gaussians, the amplitudes α_1, α_2 of the Gaussians, and the standard deviations of the Gaussians σ_1, σ_2, as well as a constant c to normalize the continuum:

$$F(\lambda) = \alpha_1 \exp\left[-\frac{(\lambda - \lambda_{1,\mathrm{rest}}(1+z))^2}{2\sigma_1^2}\right] + \alpha_2 \exp\left[-\frac{(\lambda - \lambda_{2,\mathrm{rest}}(1+z))^2}{2\sigma_2^2}\right] + c, \quad (1)$$

where $\lambda_{1,\mathrm{rest}}$ and $\lambda_{2,\mathrm{rest}}$ are the rest-frame wavelengths of the emission lines chosen. This model was fit to the spectral data and uncertainties within a narrow range around the emission

59 https://pypeit.readthedocs.io/en/release/calibrations/wave_calib.html

60 Although standard star observations of BD+75325 were taken on the night of 2022 November 13, PypeIt faced an internal error in the generation of the sensitivity file using this standard star, and the issue was raised to the PypeIt team (J. Hennawi and X. Prochaska 2026, private communications)

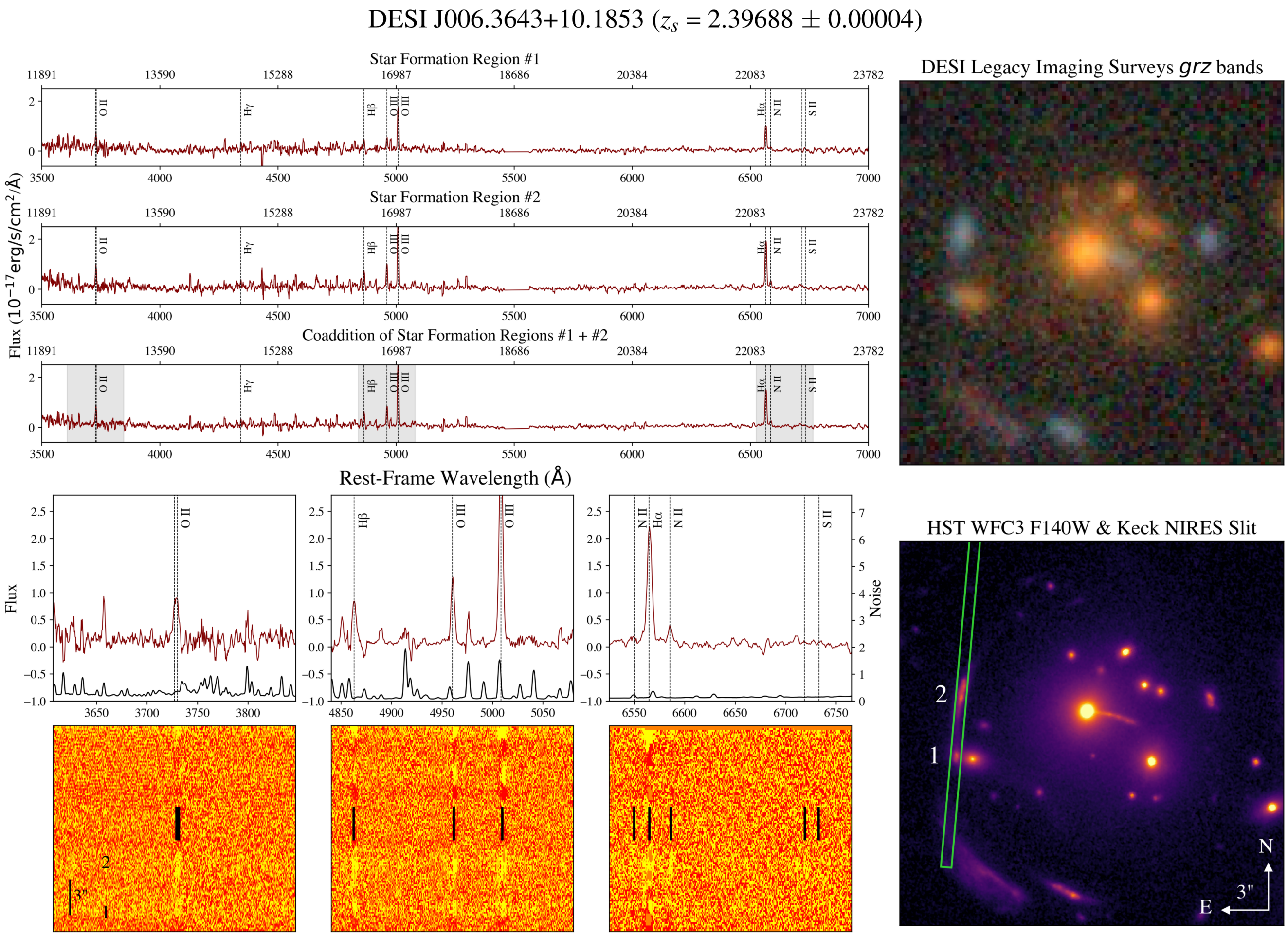

Figure 1. DESI J006.3643+10.1853. Left Column: the first and second rows show the spectra for each source image #1 and #2. The third row shows the weighted coaddition of the source image pair. The spectra in these panels are smoothed with a kernel of 10 pixels. The fourth row shows the zoom-in for individual emission lines (maroon), alongside the error spectrum (black), with a convolution kernel of 5 pixels. The error spectrum is provided on a separate scale for clarity. We show the 2D spectra in the bottom row, with black lines showing the alignment with the zoomed-in emission lines on the fourth row above. The locations of the source arcs are indicated ("1" and "2" in black) in the 2D spectra. The spatial separation of the star-forming regions in 2D spectra (note the scale bar corresponding to 3″) matches the separation in the HST F140W image. Finally, for the negative signals of the spectral features, the bright pixels above and below to them (especially prominent for [O III] doublet) are due to an artifact of the PypeIt 2D coaddition pipeline. Right Column: we show the discovery image from the DESI DR9 Legacy Surveys Imaging (*grz* bands) and the HST F140W image with the slit orientation (green). The source arcs are labeled as "1" and "2" in white. The length of the compass corresponds to 3″.

lines, using SciPy's `curve_fit` routine. The final redshift results alongside the measured uncertainties are shared in Section 4.

4. Results

We present the six lensing systems for which we have successfully obtained the source redshifts from Keck NIRES spectra, ranging from 1.67511 to 3.33185 in Section 4.1–4.6. The results are summarized in Table 2, alongside DESI spectra of the lens galaxies and other source galaxies with emission features within the DESI optical range, for completeness. The uncertainties from redshift fitting for each system, of order O(10^{-4}) to O(10^{-5}), are also provided. Since these uncertainties are small, we also note possible systematic uncertainties from PypeIt wavelength calibration. We find an rms uncertainty of <0.2 pixels for all systems tested. This corresponds to a maximum uncertainty of 0.6 Å, which would cause a maximum of O(10^{-4}) systematic error in redshift. For DESI redshifts, as described in DESI Collaboration et al. 2024 (D24), random uncertainties vary. For DESI BGSs ($z < 0.4$, with $z_{\rm med} \sim 0.2$) uncertainties are $\sigma_z = 0.00003(1 + z)$ (D24, Table 6). For LRGs ($0.4 < z < 1.1$), the uncertainties are estimated to be $\sigma_z = 0.00014(1 + z)$ (D24, Table 5). Finally, for ELGs ($0.6 < z < 1.6$), such as the two source galaxies observed by DESI in Table 2, we have $\sigma_z = 0.000026(1 + z)$ (D24, Table 5).

The spectroscopic redshifts for the lenses from the DESI Strong Lens Secondary Target program (described further in Paper II, X. Huang et al. 2025b) is shown for all systems except for DESI J094.5639+50.3059 and DESI J023.0157–16.0040. For the former, we show our redshift result from the Kast spectrograph on the 3 m Shane Telescope at the Lick Observatory on 2022 Feb 6, for which K.-V. H. Tran et al. (2022) also reported the same value. Given that these are elliptical galaxies, these spectroscopic redshifts agree well with photometric redshifts from R. Zhou et al. (2020). The two systems (DESI J023.0157–16.0040 and DESI J024.1631+00.1384) for which we have not secured the source redshifts with Keck NIRES only

Table 2
Redshift Results

System Name	z_d	z_s	σ_{z_s}
DESI J006.3643+10.1853	0.4631[a]	**2.39688**	**± 0.00004**
		1.3143[a]	± 0.00006[a]
DESI J023.0157–16.0040	…	1.5818[a]	± 0.00007[a]
DESI J024.1631+00.1384	0.3445[a]	…	…
DESI J094.5639+50.3059	0.522[b]	**3.33185**	**± 0.00010**
DESI J133.3800+23.3652	0.3053[a]	**2.18858**	**± 0.00002**
DESI J154.5307–00.1368	0.3718[a]	**1.73735, 1.73885**	**± 0.00004, 0.00006**
DESI J165.4754–06.0423	0.4834[a]	**1.67511**	**± 0.00005**
DESI J215.2654+00.3719	0.6566[a]	**2.20645**	**± 0.00035**

Notes. We report redshifts z_s of two separate sources for DESI J006.3643+10.1853 (see Section 4.1). We report two redshifts z_s for two star-forming knots within the same source for DESI J154.5307–00.1368 (see Section 4.4). The redshifts in bold are determined by Keck NIRES and are presented in detail in this work.
[a] Redshifts determined by DESI.
[b] Redshift determined from Lick.

had 600 s of exposure at higher airmass (about 1.6), shorter than the other systems (1200–3600 s), at airmasses of about 1.1–1.4. DESI J023.0157–16.0040 was later targeted successfully by DESI at the limits of its optical range, and the source redshift was determined to be 1.5818. DESI J024.1631+00.1384 will be targeted again in future observations.

4.1. DESI J006.3643+10.1853[61]

This system was discovered in H21, and the Legacy Imaging Surveys image was given a human inspection score of 2.5. In H21, the lens candidate systems with a human scores of 2 or 2.5 were given a C grade, but they stated that any system with a human score of 2.5 is at least a likely lensing system. In the DESI Legacy Surveys image (Figure 1), there are four arclets with very similar blue colors, even though they do not form a "classic" quad pattern. But this is not a surprise, given that the lens appears to be at least a group or a small cluster. The HST image confirms that three of the four suspected blue lensed images indeed have the appearance of lensed arcs, curving toward the brightest galaxy in the group, with each arc having two star formation "knots." The fourth arc appears to be a rare prominent radial arc (see, e.g., T. Broadhurst et al. 2000) near and pointing toward the brightest galaxy in the group. Keck NIRES spectroscopy now provides the redshift of the brightest lensed image. In Figure 1, we find clear evidence of the emission features Hα, [O II], [O III], Hβ, and [N II] in both the 1D and 2D spectra. The source redshift is determined to be $z_s = 2.39688$. The 1D spectra of the two knots are both shown in Figure 1 (which are at the same redshift as expected), along with their coaddition. This lensed source is among the brightest sources targeted in this Keck program. Besides the emission features, faint traces corresponding to the continuum of the source spectra can be seen in the 2D spectra (Figure 1). K.-V. H. Tran et al. (2022) reported the same source redshift of 2.396 for this system, though they did not show the spectra. There also appears to be a faint reddish arc to the SE of the Legacy Surveys image. This reddish arc is confirmed by HST, and has DESI spectra with a strong [O II] feature. The redshift of this second lensed source is at $z = 1.3143$.

[61] www.legacysurvey.org/viewer/?ra=006.36439&dec=+10.1853&layer=ls-dr9&pixscale=0.262&size=101&zoom=16

4.2. DESI J094.5639+50.3059[62]

DESI J094.5639+50.3059 was given an A grade in H21, owing to the clear presence of the main arc to the west of the foreground galaxy and a counterarc on the opposite side (Figure 2). We observed this system using the Kast spectrograph on the 3 m Shane Telescope at the Lick Observatory on 2022 February 6. We determined the lens redshift to be $z_d = 0.522$ based on clear Ca H&K, G, and Mg absorption lines. But we were unable to obtain the source redshift using Kast at Lick. The lens redshift reported by K.-V. H. Tran et al. (2022) is in agreement with this. For the lensed source, from our Keck NIRES spectra, we find clear evidence of [O II], [O III], and Hβ emissions in the 1D and 2D spectra, not just for the coaddition but also for the individual images of the knot at the tips of the main arc. There could also be a detection of a Mg II emission line, though it aligns with the noise (in black) and is not visible in the 2D spectrum. It has the highest source redshift in this paper, at $z_s = 3.33185$. This system has been modeled in Paper V (see X. Huang et al. 2025a).

4.3. DESI J133.3800+23.3652[63]

DESI J133.3800+23.3652 was given a B grade in H21. The spectra of the source arcs show evidence of strong Hα, Hβ, [O II], and [O III] doublet features in the coadded 1D and 2D spectra (Figure 3). The high SNR in this system allows us to infer the presence of the much weaker [N II] and [S II] features as well. We determine the source redshift of this system to be $z_s = 2.18858$. The two source images on opposite sides of the foreground galaxy have the same redshifts, providing further support for the lensing nature of this system. DESI J133.3800+23.3652 reduction faced a unique PypeIt error in which a portion of the 1D spectrum from the automatically detected lens galaxy was copied onto the trace corresponding to the second source image. In order to suppress this unusual behavior, PypeIt automatic object detection was turned off.[64] This enabled us to perform a manual extraction on the source galaxy spectra for both images of the star-forming knot using

[62] www.legacysurvey.org/viewer/?ra=094.5639&dec=+50.3059&layer=ls-dr9&pixscale=0.262&size=101&zoom=16
[63] www.legacysurvey.org/viewer/?ra=133.3800&dec=+23.3652&layer=ls-dr9&pixscale=0.262&size=101&zoom=16
[64] This issue was also raised to and acknowledged by the PypeIt team (X. Prochaska 2026, Private communications)

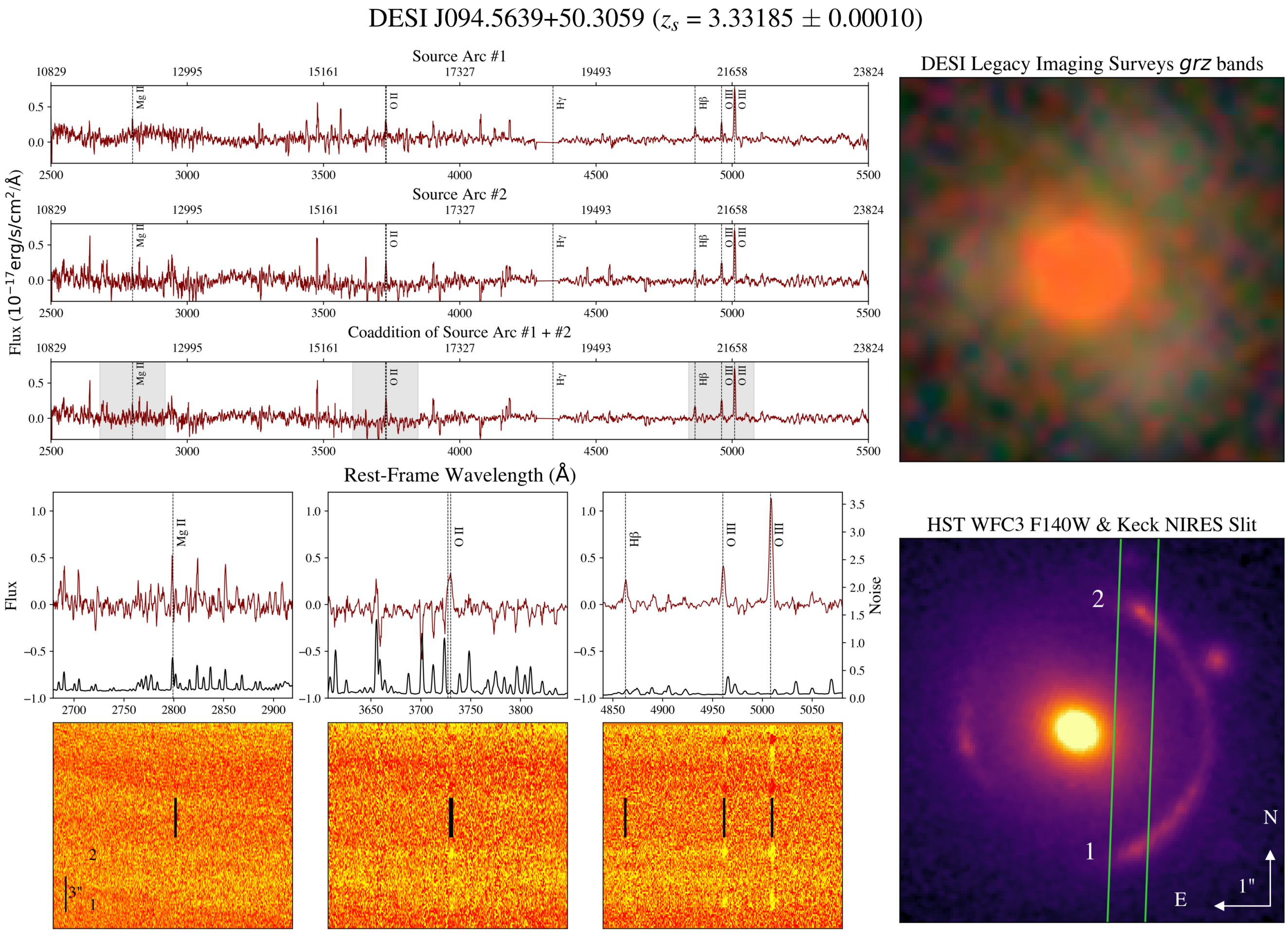

Figure 2. DESI J094.5639+50.3059. For the arrangement of the panels, see the caption of Figure 1.

PypeIt's manual extraction feature. The manual extraction routine was then adopted for all other systems as well, as mentioned in Section 3.2. There is a second lensed source to the east of the measured lensed source that falls into the slit. However, we were unable to locate any emission features for that source within our 1200 s exposure.

4.4. DESI J154.5307–00.1368[65]

This system was given a B grade in H20, on account of the faint blue arc to the SW of the foreground galaxy (Figure 4). The NIRES 2D spectra show a strong signal for Hα emission, and next to it, a detection of the [N II] emission line. The presence of Hβ is weaker but clear, yet we do not find an obvious detection of the [O III] doublet. Finally, there may be a hint of the [O II] doublet in the 2D spectrum, which can also been seen in one of the coadded 1D spectra (second row in Figure 4), at $\sim 2\sigma$. We note that this feature is only found in one of the two star-forming regions, which may be due to low signal-to-noise ratio and/or the two knots having different oxygen compositions. The redshift of the system is determined to be $z_s = 1.73810$. Note that the two tips of the arc are two *different* star formation regions. They have slightly different redshifts, at 1.73885 and 1.73735, for the eastern and western knot, respectively (labeled as knot #1 and #2 in Figure 4). We see clear evidence for this difference in the Hα emission feature in both 2D and 1D spectra. The Hβ emission appears to show the same difference. This difference in redshift corresponds to a line-of-sight velocity difference of 164.2 km s^{-1} (Equation (10), D. W. Hogg 1999). The existence of a velocity difference indicates these may be two separate knots, rather than multiple images of the same knot. Lens modeling of this system is forthcoming, and it may shed more light on the specific lensing configuration. For now, we expect that the system is either a singly lensed arc (the targeted southwest arc) or an "inclined double configuration" (P. Saha & L. L. R. Williams 2003), where the second arc is the source north of the lens galaxy. Depending on the outcome, one interpretation may be that separate, lensed knots are on opposite ends of the galaxy, and we detect the velocity difference due to galactic rotation. We average the redshifts of the two knots to determine the source redshift. Approximately 5″ to the north, there appears to be an arclet that may be another lensed image of the same background galaxy. We will target this object in future spectroscopic observations.

[65] www.legacysurvey.org/viewer/?ra=154.5307&dec=-00.1368&layer=ls-dr9&pixscale=0.262&size=101&zoom=16

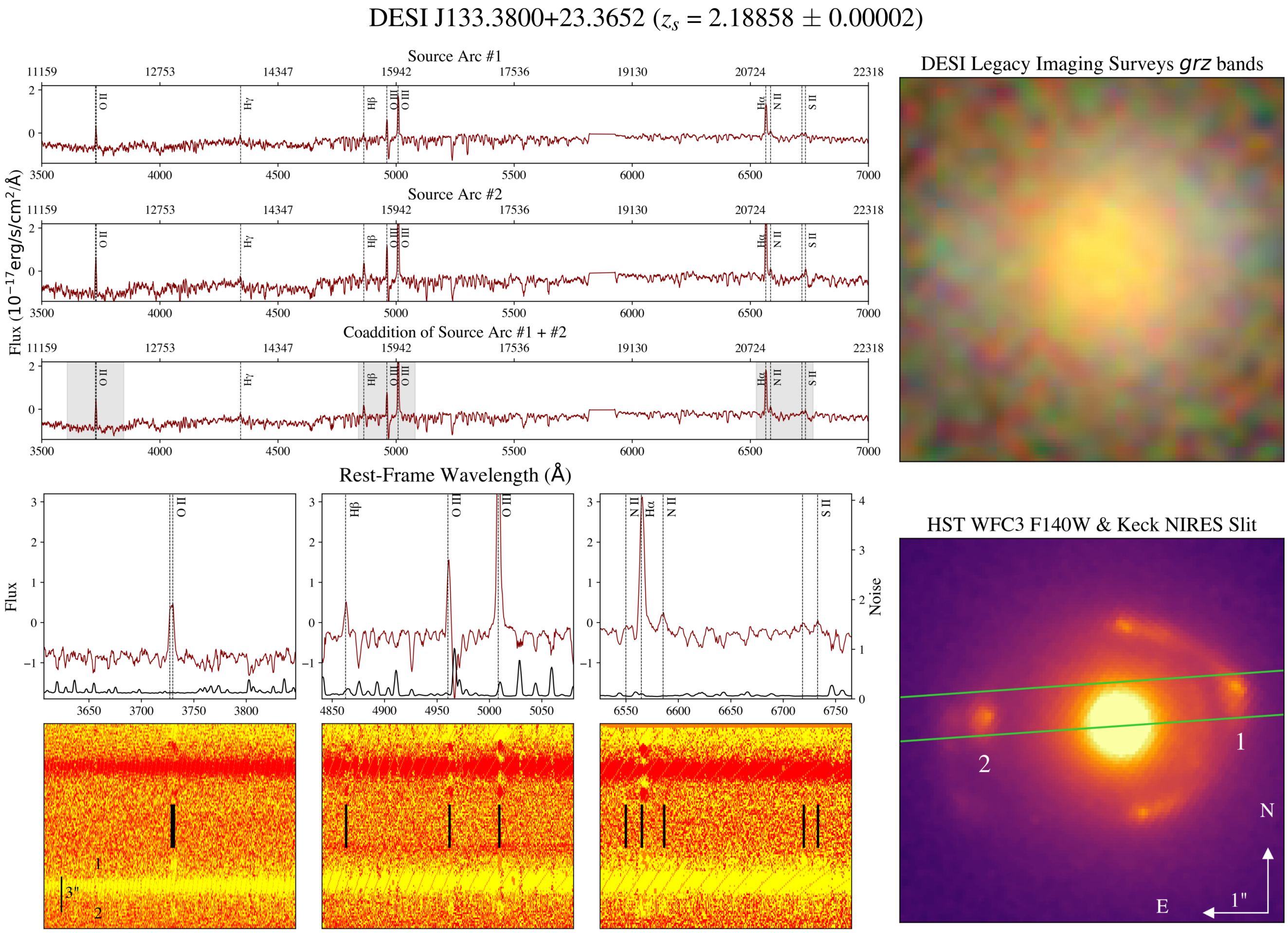

Figure 3. DESI J133.3800+23.3652. For the arrangement of the panels, see the caption of Figure 1.

4.5. DESI J165.4754–06.0423[66]

DESI J165.4754–06.0423 was given a grade C in H21, with a human score of 2.5, which indicates at least a likely candidate (see Section 4.1). We determine the source redshift to be $z_s = 1.67511$. It is the lowest-redshift source galaxy in this work, with the [O II] doublet emission feature lying just beyond the optical edge of DESI spectroscopy. From the NIRES spectra, clear Hα, [N II], and Hβ signals, alongside the brighter of the [O III] doublet and a possible weak [S II] and Hγ signal, enable us to secure the redshift of the source galaxy. The bump in the 1D coadded spectrum between the [S II] doublet is due to imperfect subtraction of a bright sky line. This can be seen as a jump at that wavelength in the noise spectrum, which is only present in one of the two individual 1D spectra (Source Arc #2 in Figure 5).

4.6. DESI J215.2654+00.3719[67]

DESI J215.2654+00.3719 is a grade A candidate in H20, with two prominent blue arcs around an elliptical galaxy. This system has the faintest star-forming regions in this program, with the brightest knot in the arcs being 22.8 mag in HST F140W.[68] It was observed with 2400 s of exposure because it was near the end of night. With careful inspection, we have found two weak features in the 2D spectrum, with both a visible positive and negative signal to ensure they are not due to noise (Figure 6). We reason that they must be the strongest features in the NIR range, and have conducted tests to fit them for Hα, [O III], and [O II] in order. We find that the spacing between them exactly matches that between Hα and the brighter of the [O III] doublet, which are generally the two emission features with the clearest detections in the other NIR spectra presented in this work. This places the source galaxy at a redshift of $z_s = 2.20645$. The nondetection of other emission features such as [O II], Hβ, [N II], and [S II] is unsurprising due to the intrinsic relative faintness of these emission lines compared to the faint detected Hα and [O III] features and given the intrinsically low brightness of the star-forming regions (magnitudes of 24.15 and 24.41; see Table 1). The zoom-in views of the 1D spectrum and 2D features are shown in Figure 6.

66 www.legacysurvey.org/viewer/?ra=165.4754&dec=-06.0423&layer=ls-dr9&pixscale=0.262&size=101&zoom=16
67 www.legacysurvey.org/viewer/?ra=215.2654&dec=+00.3719&layer=ls-dr9&pixscale=0.262&size=101&zoom=16

68 We did not target the brightest feature in the F140W cutout image near the top center (Figure 6, lower right panel). Given its reddish color in the Legacy Surveys *grz* image, we suspect this feature likely corresponds to a small interloper or satellite galaxy. We will address the nature of this object in future follow-up observations.

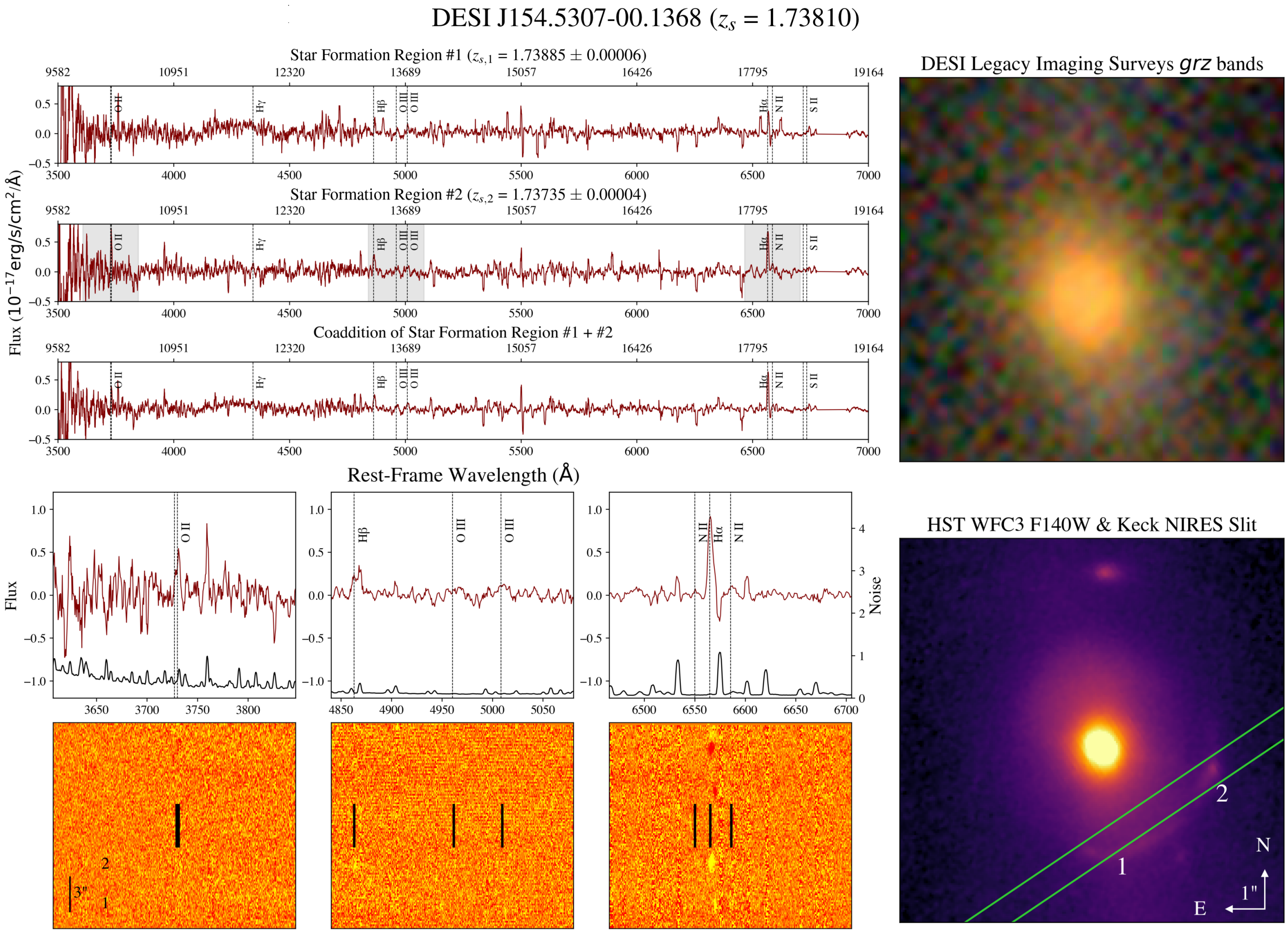

Figure 4. DESI J154.5307–00.1368. For the arrangement of the panels, see the caption of Figure 1. Note that, in the 2D zoom-in, the Hα emission features corresponding to the two star-forming knots do not align exactly in the spectral direction, indicating slightly different redshifts for knot #1 and #2 at $z_{s,1} = 1.73885$ and $z_{s,2} = 1.73735$, respectively. For this system, the zoom-in panels in the fourth row highlight the 1D spectrum of star formation region #2 (corresponding to the gray highlighted areas in the second row) and not the coaddition.

5. Discussion and Conclusion

5.1. Further Analysis

The focus of this paper is to obtain redshifts, which are necessary for setting the overall scale for the lens mass profiles through lens modeling (Paper V; X. Huang et al. 2025a). However, the spectra contain significant information beyond redshift determination. Other possible avenues for further research include analysis of high-redshift galaxy star formation rates through measurement of equivalent widths of lines such as Hα and Hβ (e.g., R. C. Livermore et al. 2015; V. Patrício et al. 2018; D. Nagy et al. 2023). Given that the continuum is not always detected, this would represent a lower bound, which nevertheless is a useful estimate. This information is also essential for estimating supernova rates, and can be used to identify ideal systems for lensed-supernova searches (e.g., Y. Shu et al. 2018, 2021). Finally, given that the strong lensing systems in the paper magnify high-redshift source galaxies at redshifts $z \sim 1.7$–3.3, their metallicities and galaxy evolution (e.g., D. P. Stark et al. 2013; T.-T. Yuan et al. 2013; V. Patrício et al. 2019; X. He et al. 2024) could be studied, along with reionization in general, through further Lyα studies (T. E. Rivera-Thorsen et al. 2017; G. Khullar et al. 2021).

5.2. Conclusion

We present and analyze Keck NIRES spectra of strong lensing systems discovered in the DESI Legacy Imaging Surveys using residual neural networks. Redshifts from this program can be used for various strong lensing applications, such as characterizing the selection function of the neural network used, as well as converting geometrical parameters to physical ones. Additionally, this paper demonstrates the potential of the neural network lens sample for discoveries of high-redshift galaxies, galaxy formation studies, and understanding reionization. The candidate systems used have unambiguous lensing features that have been confirmed by our Hubble Space Telescope program (GO-15867, PI: Huang).

We targeted the lensed sources of these systems because they were beyond the optical range of DESI, specifically when the [O II] doublet at 3727 Å is redshifted beyond 9800 Å (A. G. Adame et al. 2024), at $z \sim 1.6$. The exception is DESI J023.0157–16.0040, where the [O II] doublet is barely within range and was successfully observed by DESI to have a redshift of 1.5818. We have succeeded in measuring the lensed source redshifts for six (with an exposure time of 1200–3600 s) of seven other observed systems, with z_s between = 1.67511 and 3.33185. Two each of these six systems were given grades

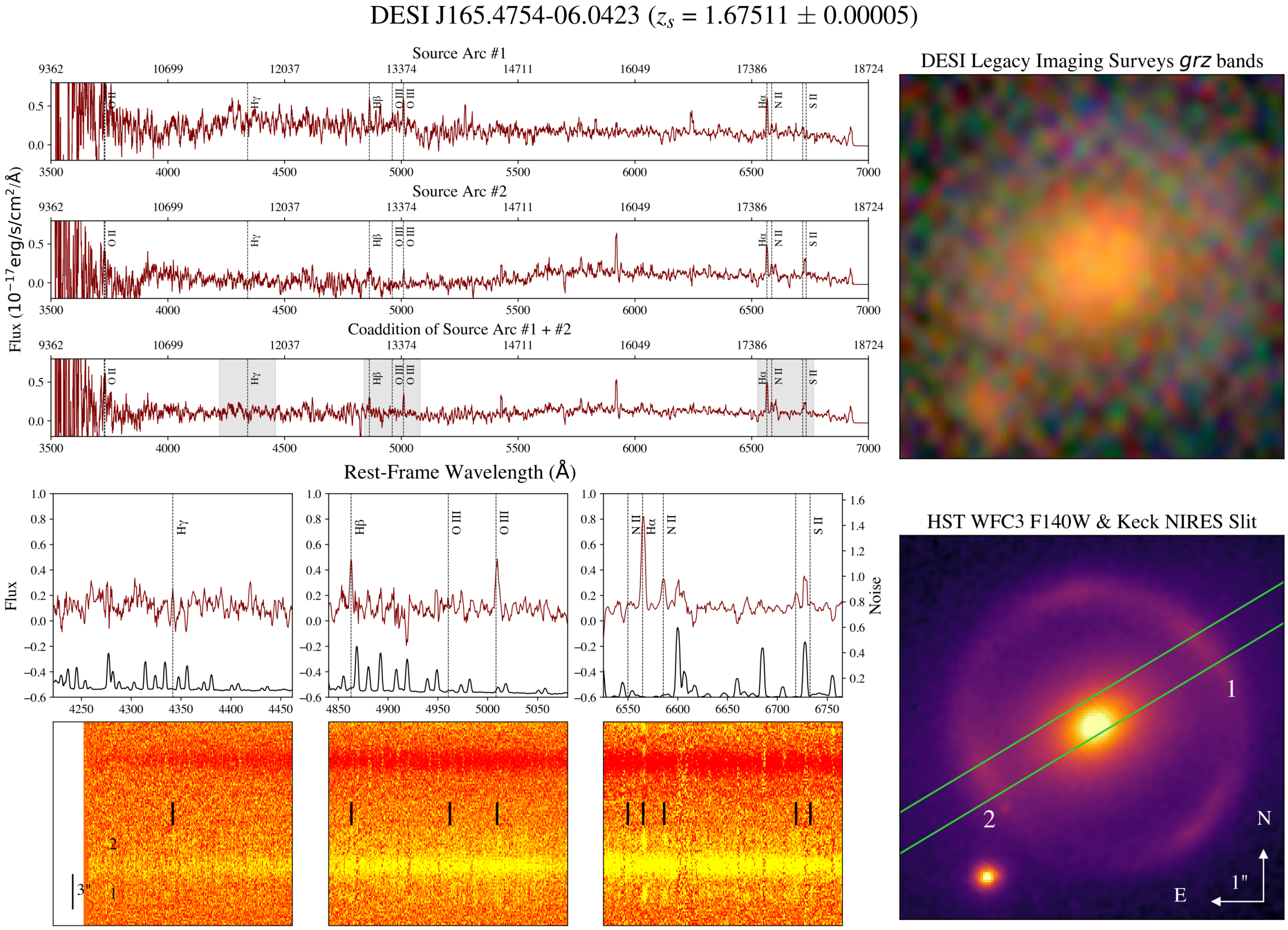

Figure 5. DESI J165.4754–06.0423. For the arrangement of the panels, see the caption of Figure 1.

A, B, and C (with human inspection scores of 4, 3, and 2.5, respectively) in our lens searches (X. Huang et al. 2020, 2021, where we pointed out that candidates with a score of 2.5 or above are at least likely lenses). The two systems for which we did not obtain the source redshifts with Keck NIRES had considerably shorter exposure times (600 s) and were at higher airmass (∼1.6). DESI J024.1631+00.1384 will be targeted in future observations. This is a relatively small sample, and we will present larger samples of confirmed systems in the DESI Strong Lens Foundry series. Nevertheless, this is a promising first assessment that attests to the quality of our lens candidates found in the DESI Legacy Imaging Surveys. These NIR spectroscopic observations show great promise for obtaining lensing systems at high redshifts, for which the strongest spectral features of the lensed sources are beyond the optical range.

Though the main objective of this program is to obtain redshifts, the spectra we obtained clearly have sufficient signal-to-noise ratios for follow-up investigations, in particular, measuring the equivalent width of the most prominent emission lines and determining metallicity ratios. This would allow us to estimate the star formation rates and therefore supernova rates in the lensed source galaxies, and to study the metallicity and formation process of high-redshift galaxies. That work is beyond the scope of this paper, and may be carried out in a future study.

For systems observed with at least one full ABBA dither pattern (1200 s), Keck NIRES achieves a 100% success rate in obtaining redshifts for the lensed sources. In addition to NIR spectroscopy, another possible method for follow-up is to use deep optical spectroscopy to identify weaker spectral lines (e.g., DESI J253.2534+26.8843; A. Cikota et al. 2023). In future follow-up observations, the comparison between the efficiencies of NIR spectroscopy and deep optical spectroscopy for high-redshift lensed sources could be investigated further with our large sample of lens candidates.

Acknowledgments

This work was supported in part by the Director, Office of Science, Office of High Energy Physics of the US Department of Energy under contract No. DE-AC025CH11231. This research used resources of the National Energy Research Scientific Computing Center (NERSC), a U.S. Department of Energy Office of Science User Facility operated under the same contract as above and the Computational HEP program in The Department of Energy's Science Office of High Energy Physics provided resources through the "Cosmology Data Repository" project (grant No. KA2401022). S.A. acknowledges the opportunities provided by the Undergraduate Research Apprenticeship Program (URAP) at the University of California, Berkeley. X.H. acknowledges the University of

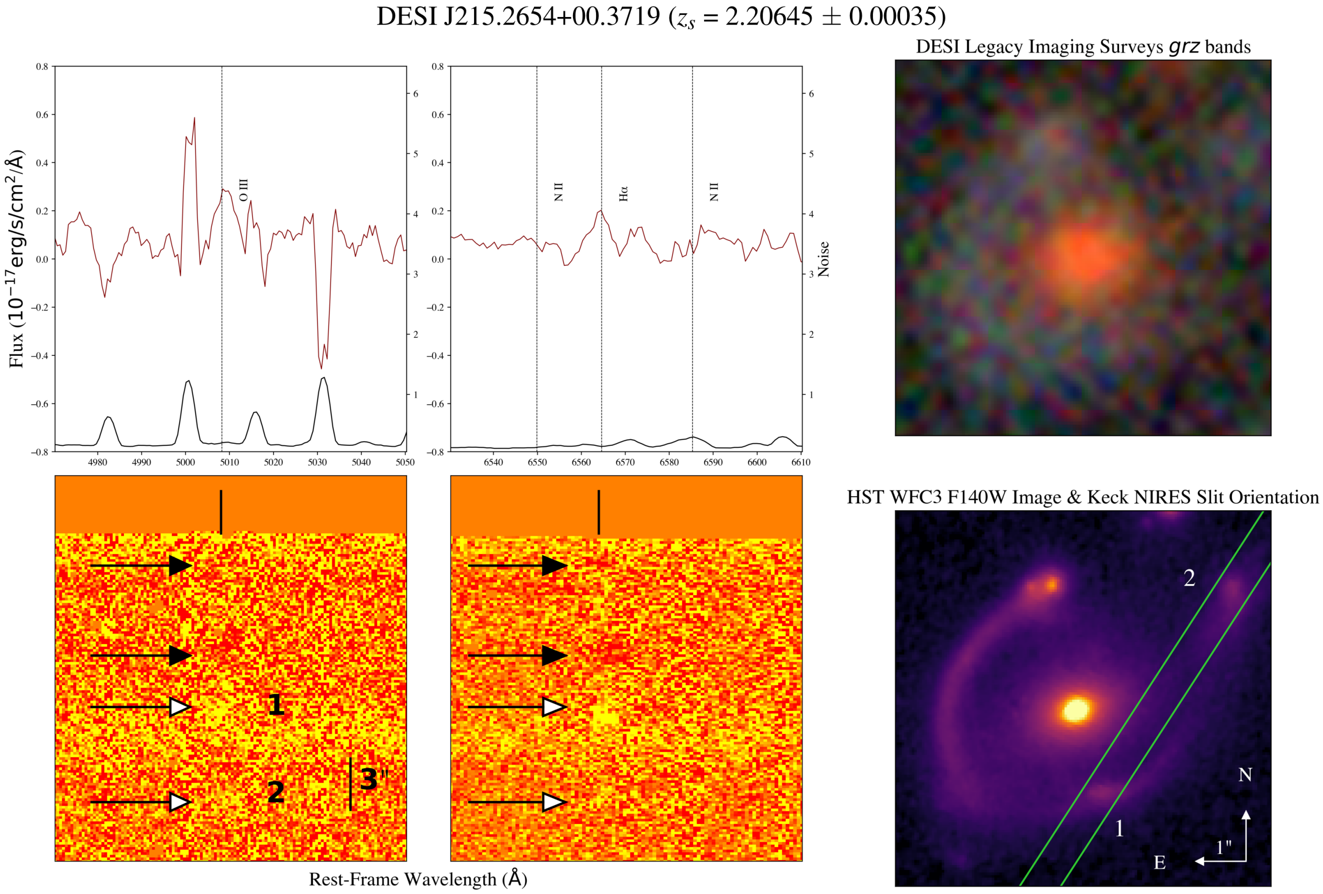

Figure 6. DESI J215.2654+00.3719. Left Column: in the top row, the left and right panels show the zoom-in for the coadded 1D emission lines [O III] and Hα (maroon), respectively, alongside the error spectrum (black), with a convolution kernel of width 2 pixels. The 2D spectra are presented in the bottom row, with vertical lines near the top showing the alignment with 1D emission lines. The locations of the source arcs are indicated ("1" and "2" in black) in the lower left 2D spectrum. In the 2D spectra, we highlight the positive (white arrowheads) and negative signals (black arrowheads) from the dither pattern. The presence of both distinguishes the pattern from noise. The spatial separation of the star-forming regions in 2D spectra matches that in the HST F140W image (4.″86). Also note the presence of the continuum of the lensing galaxy spectrum between emission features #1 and #2. Right Column: we show the discovery image from the DESI DR9 Legacy Surveys Imaging (*grz* bands) and the HST F140W image with the slit orientation (green). The source arcs are labeled as "1" and "2" in white.

San Francisco Faculty Development Fund. Support for HST program 15867 was provided by NASA through a grant from the Space Telescope Science Institute, which is operated by the Association of Universities for Research in Astronomy, Inc., under NASA contract NAS 5-26555. We thank the creators of PypeIt for support with usage of the package. We also thank the Support Astronomers and the technical staff of the W. M Keck Observatory. We recognize the significant cultural role of Maunakea within the indigenous Hawaiian community, and we appreciate the opportunity to conduct observations from this revered site.

The Legacy Surveys consist of three individual and complementary projects: the Dark Energy Camera Legacy Survey (DECaLS; Proposal ID #2014B-0404; PIs: David Schlegel and Arjun Dey), the Beijing-Arizona Sky Survey (BASS; NOAO Prop. ID #2015A-0801; PIs: Zhou Xu and Xiaohui Fan), and the Mayall z-band Legacy Survey (MzLS; Prop. ID #2016A-0453; PI: Arjun Dey). DECaLS, BASS, and MzLS together include data obtained, respectively, at the Blanco telescope, Cerro Tololo Inter-American Observatory, NSF's NOIRLab; the Bok telescope, Steward Observatory, University of Arizona; and the Mayall telescope, Kitt Peak National Observatory, NOIRLab. Pipeline processing and analyzes of the data were supported by NOIRLab and the Lawrence Berkeley National Laboratory (LBNL). The Legacy Surveys project is honored to be permitted to conduct astronomical research on Iolkam Du'ag (Kitt Peak), a mountain with particular significance to the Tohono O'odham Nation. NOIRLab is operated by the Association of Universities for Research in Astronomy (AURA) under a cooperative agreement with the National Science Foundation. LBNL is managed by the Regents of the University of California under contract to the U.S. Department of Energy. This project used data obtained with the Dark Energy Camera (DECam), which was constructed by the Dark Energy Survey (DES) collaboration. Funding for the DES Projects has been provided by the U.S. Department of Energy, the U.S. National Science Foundation, the Ministry of Science and Education of Spain, the Science and Technology Facilities Council of the United Kingdom, the Higher Education Funding Council for England, the National Center for Supercomputing Applications at the University of Illinois at Urbana-Champaign, the Kavli Institute of Cosmological Physics at the University of Chicago, Center for Cosmology and Astro-Particle Physics at the Ohio State University, the Mitchell Institute for Fundamental Physics and Astronomy at

Texas A&M University, Financiadora de Estudos e Projetos, Fundação Carlos Chagas Filho de Amparo à Pesquisa do Estado do Rio de Janeiro, Conselho Nacional de Desenvolvimento Científico e Tecnológico, the Ministério da Ciência, Tecnologia e Inovacão, the Deutsche Forschungsgemeinschaft, and the Collaborating Institutions in the Dark Energy Survey. The Collaborating Institutions are Argonne National Laboratory, the University of California at Santa Cruz, the University of Cambridge, Centro de Investigaciones Enérgeticas, Medioambientales y Tecnológicas-Madrid, the University of Chicago, University College London, the DES-Brazil Consortium, the University of Edinburgh, the Eidgenössische Technische Hochschule (ETH) Zürich, Fermi National Accelerator Laboratory, the University of Illinois at Urbana-Champaign, the Institut de Ciències de l'Espai (IEEC/CSIC), the Institut de Física d'Altes Energies, Lawrence Berkeley National Laboratory, the Ludwig-Maximilians Universität München and the associated Excellence Cluster Universe, the University of Michigan, NSF's NOIRLab, the University of Nottingham, the Ohio State University, the University of Pennsylvania, the University of Portsmouth, SLAC National Accelerator Laboratory, Stanford University, the University of Sussex, and Texas A&M University. BASS is a key project of the Telescope Access Program (TAP), which has been funded by the National Astronomical Observatories of China, the Chinese Academy of Sciences (the Strategic Priority Research Program "The Emergence of Cosmological Structures" Grant # XDB09000000), and the Special Fund for Astronomy from the Ministry of Finance. The BASS is also supported by the External Cooperation Program of the Chinese Academy of Sciences (Grant #114A11KYSB20160057) and the Chinese National Natural Science Foundation (Grants #12120101003 and #11433005). The Legacy Survey team makes use of data products from the Near-Earth Object Wide-field Infrared Survey Explorer (NEOWISE), which is a project of the Jet Propulsion Laboratory/California Institute of Technology. NEOWISE is funded by the National Aeronautics and Space Administration. The Legacy Surveys imaging of the DESI footprint is supported by the Director, Office of Science, Office of High Energy Physics of the U.S. Department of Energy under Contract No. DE-AC02-05CH1123, by the National Energy Research Scientific Computing Center, a DOE Office of Science User Facility under the same contract; and by the U.S. National Science Foundation, Division of Astronomical Sciences, under Contract No. AST-0950945 to NOAO.

This research used data obtained with the Dark Energy Spectroscopic Instrument (DESI). The construction and operations of DESI are managed by the Lawrence Berkeley National Laboratory. This material is based upon work supported by the U.S. Department of Energy, Office of Science, Office of High-Energy Physics, under Contract No. DE'AC02'05CH11231, and by the National Energy Research Scientific Computing Center, a DOE Office of Science User Facility under the same contract. Additional support for DESI was provided by the U.S. National Science Foundation (NSF), Division of Astronomical Sciences under Contract No. AST-0950945 to the NSF's National Optical-Infrared Astronomy Research Laboratory; the Science and Technology Facilities Council of the United Kingdom; the Gordon and Betty Moore Foundation; the Heising-Simons Foundation; the French Alternative Energies and Atomic Energy Commission (CEA); the National Council of Science and Technology of Mexico (CONACYT); the Ministry of Science and Innovation of Spain (MICINN), and by the DESI Member Institutions: www.desi.lbl.gov/collaborating-institutions. The DESI collaboration is honored to be permitted to conduct scientific research on Iolkam Du'ag (Kitt Peak), a mountain with particular significance to the Tohono O'odham Nation. Any opinions, findings, and conclusions or recommendations expressed in this material are those of the author(s) and do not necessarily reflect the views of the U.S. National Science Foundation, the U.S. Department of Energy, or any of the listed funding agencies.

ORCID iDs

Shrihan Agarwal https://orcid.org/0000-0002-2350-4610
Xiaosheng Huang https://orcid.org/0000-0001-8156-0330
W. Sheu https://orcid.org/0000-0003-1889-0227
C.J. Storfer https://orcid.org/0000-0002-0385-0014
M. Tamargo-Arizmendi https://orcid.org/0009-0008-0518-8045
S. Tabares-Tarquinio https://orcid.org/0000-0003-3533-5890
D.J. Schlegel https://orcid.org/0000-0002-5042-5088
A. Cikota https://orcid.org/0000-0001-7101-9831
Arjun Dey https://orcid.org/0000-0002-4928-4003
A. Filipp https://orcid.org/0000-0003-4701-3469
E. Jullo https://orcid.org/0000-0002-9253-053X
K.J. Kwon https://orcid.org/0000-0001-9802-362X
S. Perlmutter https://orcid.org/0000-0002-4436-4661
Y. Shu https://orcid.org/0000-0002-9063-698X
E. Sukay https://orcid.org/0000-0002-1106-4881
N. Suzuki https://orcid.org/0000-0001-7266-930X
J. Aguilar https://orcid.org/0000-0003-0822-452X
S. Ahlen https://orcid.org/0000-0001-6098-7247
S. BenZvi https://orcid.org/0000-0001-5537-4710
D. Brooks https://orcid.org/0000-0002-8458-5047
P. Doel https://orcid.org/0000-0002-6397-4457
J. E. Forero-Romero https://orcid.org/0000-0002-2890-3725
E. Gaztañaga https://orcid.org/0000-0001-9632-0815
S. Gontcho A Gontcho https://orcid.org/0000-0003-3142-233X
G. Gutierrez https://orcid.org/0000-0003-0825-0517
K. Honscheid https://orcid.org/0000-0002-6550-2023
M. Ishak https://orcid.org/0000-0002-6024-466X
S. Juneau https://orcid.org/0000-0002-0000-2394
R. Kehoe https://orcid.org/0000-0002-7101-697X
T. Kisner https://orcid.org/0000-0003-3510-7134
S. E. Koposov https://orcid.org/0000-0003-2644-135X
M. Landriau https://orcid.org/0000-0003-1838-8528
L. Le Guillou https://orcid.org/0000-0001-7178-8868
A. de la Macorra https://orcid.org/0000-0002-1769-1640
A. Meisner https://orcid.org/0000-0002-1125-7384
R. Miquel https://orcid.org/0000-0002-6610-4836
J. Moustakas https://orcid.org/0000-0002-2733-4559
C. Poppett https://orcid.org/0000-0003-0512-5489
F. Prada https://orcid.org/0000-0001-7145-8674
I. Pérez-Ràfols https://orcid.org/0000-0001-6979-0125
E. Sanchez https://orcid.org/0000-0002-9646-8198
D. Sprayberry https://orcid.org/0000-0001-7583-6441
G. Tarlé https://orcid.org/0000-0003-1704-0781
H. Zou https://orcid.org/0000-0002-6684-3997

References

Adame, A. G., Aguilar, J., Ahlen, S., et al. 2024, AJ, 168, 58
Bajaj, V., Calamida, A., & Mack, J. 2020, Updated WFC3/IR Photometric Calibration, Instrument Science Report WFC3 2020-10, STScI https://stsci.recollectcms.com/nodes/view/7093
Bohlin, R. C., Gordon, K. D., & Tremblay, P. E. 2014, PASP, 126, 711
Bolton, A. S., Burles, S., Koopmans, L. V. E., et al. 2008, ApJ, 682, 964
Bolton, A. S., Burles, S., Koopmans, L. V. E., Treu, T., & Moustakas, L. A. 2006, ApJ, 638, 703
Bradač, M., Allen, S. W., Treu, T., et al. 2008, ApJ, 687, 959
Broadhurst, T., Huang, X., Frye, B., & Ellis, R. 2000, ApJL, 534, L15
Çağan Şengül, A. Ç., Dvorkin, C., Ostdiek, B., & Tsang, A. 2022, MNRAS, 515, 4391
Cikota, A., Bertolla, I. T., Huang, X., et al. 2023, ApJL, 953, L5
Clowe, D., Bradač, M., Gonzalez, A. H., et al. 2006, ApJL, 648, L109
Cornachione, M. A., Bolton, A. S., Shu, Y., et al. 2018, ApJ, 853, 148
Dawes, C., Storfer, C., Huang, X., et al. 2023, ApJS, 269, 61
DESI Collaboration, Aghamousa, A., Aguilar, J., et al. 2016a, arXiv:1611.00037
DESI Collaboration, Aghamousa, A., Aguilar, J., et al. 2016b, arXiv:1611.00036
DESI Collaboration, Adame, A. G., Aguilar, J., et al. 2024, AJ, 167, 62
Dey, A., Schlegel, D. J., Lang, D., et al. 2019, AJ, 157, 168
Goldstein, D. A., & Nugent, P. E. 2017, ApJL, 834, L5
Goldstein, D. A., Nugent, P. E., Kasen, D. N., & Collett, T. E. 2018, ApJ, 855, 22
Grillo, C., Suyu, S. H., Rosati, P., et al. 2015, ApJ, 800, 38
He, K., Zhang, X., Ren, S., & Sun, J. 2015, in IEEE Conf. on Computer Vision and Pattern Recognition (IEEE) 770
He, X., Wang, X., Jones, T., et al. 2024, ApJL, 960, L13
Hezaveh, Y. D., Dalal, N., Marrone, D. P., et al. 2016, ApJ, 823, 37
Hogg, D. W. 1999, arXiv:astro-ph/9905116
Huang, X., Alvarez-Garcia, D., Ubeda, M., et al. 2025a, arXiv:2512.07823
Huang, X., Baltasar, S., Ratier-Werbin, N., et al. 2026, ApJ, 998, 69
Huang, X., Inchausti, J. C., Storfer, C. J., et al. 2025b, arXiv:2509.18089
Huang, X., Morokuma, T., Fakhouri, H. K., et al. 2009, ApJ, 707, L12
Huang, X., Storfer, C., Gu, A., et al. 2021, ApJ, 909, 27
Huang, X., Storfer, C., Ravi, V., et al. 2020, ApJ, 894, 78
Huchra, J., Gorenstein, M., Kent, S., et al. 1985, AJ, 90, 691
Jullo, E., Natarajan, P., Kneib, J. P., et al. 2010, Sci, 329, 924
Kelly, P. L., Rodney, S., Treu, T., et al. 2023, ApJ, 948, 93
Khullar, G., Gozman, K., Lin, J. J., et al. 2021, ApJ, 906, 107
Kochanek, C. S. 1991, ApJ, 373, 354
Koopmans, L. V. E., & Treu, T. 2002, ApJL, 568, L5
Koopmans, L. V. E., Treu, T., Bolton, A. S., Burles, S., & Moustakas, L. A. 2006, ApJ, 649, 599
Livermore, R. C., Jones, T. A., Richard, J., et al. 2015, MNRAS, 450, 1812
Marshall, P. J., Treu, T., Melbourne, J., et al. 2007, ApJ, 671, 1196
Nagy, D., Dessauges-Zavadsky, M., Messa, M., et al. 2023, A&A, 678, A183
Patrício, V., Richard, J., Carton, D., et al. 2018, MNRAS, 477, 18
Patrício, V., Richard, J., Carton, D., et al. 2019, MNRAS, 489, 224
Pierel, J. D. R., & Rodney, S. 2019, ApJ, 876, 107
Prochaska, J., Hennawi, J., Westfall, K., et al. 2020a, JOSS, 5, 2308
Prochaska, J. X., Hennawi, J., Cooke, R., et al. 2020b, pypeit/PypeIt: Release 1.0.0, v1.0.0, Zenodo, doi:10.5281/zenodo.3743493
Rivera-Thorsen, T. E., Dahle, H., Gronke, M., et al. 2017, A&A, 608, L4
Saha, P., & Williams, L. L. R. 2003, AJ, 125, 2769
Shu, Y., Bolton, A. S., Mao, S., et al. 2018, ApJ, 864, 91
Shu, Y., Bolton, A. S., Mao, S., et al. 2021, ApJ, 919, 67
Shu, Y., Bolton, A. S., Brownstein, J. R., et al. 2015, ApJ, 803, 71
Shu, Y., Bolton, A. S., Kochanek, C. S., et al. 2016a, ApJ, 824, 86
Shu, Y., Bolton, A. S., Moustakas, L. A., et al. 2016b, ApJ, 820, 43
Shu, Y., Brownstein, J. R., Bolton, A. S., et al. 2017, ApJ, 851, 48
Stark, D. P., Auger, M., Belokurov, V., et al. 2013, MNRAS, 436, 1040
Storfer, C., Huang, X., Gu, A., et al. 2024, ApJS, 274, 16
Suyu, S. H., Goobar, A., Collett, T., More, A., & Vernardos, G. 2024, SSRv, 220, 13
Suyu, S. H., Huber, S., Ca,nameras, R., et al. 2020, A&A, 644, A162
Tessore, N., Bellagamba, F., & Metcalf, R. B. 2016, MNRAS, 463, 3115
Tran, K.-V. H., Harshan, A., Glazebrook, K., et al. 2022, AJ, 164, 148
Vanzella, E., Meneghetti, M., Caminha, G. B., et al. 2020, MNRAS, 494, L81
Vegetti, S., Koopmans, L. V. E., Bolton, A., Treu, T., & Gavazzi, R. 2010, MNRAS, 408, 1969
Walsh, D., Carswell, R. F., & Weymann, R. J. 1979, Natur, 279, 381
Wilson, J. C., Henderson, C. P., Herter, T. L., et al. 2004, SPIE, 5492, 1295
Wojtak, R., Hjorth, J., & Gall, C. 2019, MNRAS, 487, 3342
Yuan, T.-T., Kewley, L. J., & Richard, J. 2013, ApJ, 763, 9
Zhou, R., Newman, J. A., Mao, Y.-Y., et al. 2020, MNRAS, 501, 3309